

# A VO<sub>2</sub> film-based multifunctional metasurface in the terahertz band

Ziyu Liu (刘紫玉)<sup>1</sup>, Limei Qi (齐丽梅)<sup>1,2\*</sup>, Feng Lan (兰峰)<sup>3</sup>, Chuwen Lan (兰楚文)<sup>4,5</sup>, Jun Yang (杨君)<sup>1</sup>, and Xiang Tao (陶翔)<sup>1</sup>

<sup>1</sup>School of Electronic Engineering, Beijing University of Posts and Telecommunications, Beijing 100876, China

<sup>2</sup>Collaborative Innovation Center of Light Manipulations and Applications, Shandong Normal University, Jinan 250358, China

<sup>3</sup>The Yangtze Delta Region Institute (Huzhou), University of Electronic Science and Technology of China, Huzhou 313001, China

<sup>4</sup>Shenzhen Research Institute, Beijing University of Posts and Telecommunications, Shenzhen 518000, China

<sup>5</sup>School of Information and Communication Engineering, Beijing University of Posts and Telecommunications, Beijing 100876, China

\*Corresponding author: [qilimei1204@163.com](mailto:qilimei1204@163.com)

Received September 4, 2021 | Accepted October 14, 2021 | Posted Online November 16, 2021

We proposed a multifunctional terahertz metasurface based on a double L-shaped pattern and a vanadium dioxide (VO<sub>2</sub>) film separated by polyimide. When the VO<sub>2</sub> film is an insulator, a dual-band electromagnetically induced transparency effect is obtained, and the physical mechanism is investigated based on the current distribution and “two-particle” model. When the VO<sub>2</sub> film is a metal, a dual-band linear-to-circular polarization converter, in which the  $y$ -polarized linear wave can be effectively converted to left-handed circularly polarized (LCP) and right-handed circularly polarized simultaneously in different bands, can be achieved. By arranging the metal pattern rotating 30°, a multifunctional antenna can be obtained. When the VO<sub>2</sub> is an insulator, the radiation of the LCP wave is divided into four beams, with two beams reflected and two beams transmitted. When the VO<sub>2</sub> is in the metallic state, we can only get the co-polarized reflected wave with a 21° angle. Moreover, in our design, the VO<sub>2</sub> film does not need lithography to obtain certain patterns, which improves the convenience of fabrication and experiment. Our design opens a new way for the development of multifunctional terahertz devices and has potential applications in the terahertz communication field.

**Keywords:** terahertz; VO<sub>2</sub>; antenna; metasurface.

**DOI:** [10.3788/COL202220.013602](https://doi.org/10.3788/COL202220.013602)

## 1. Introduction

With the rapid development of terahertz (THz) science and technology, THz devices have aroused great interests<sup>[1–3]</sup>. Metasurfaces with the properties of simple structure, easy manufacture, low profile, and convenient integration<sup>[4–7]</sup>, have been widely researched in THz filters<sup>[8,9]</sup>, perfect absorbers<sup>[10,11]</sup>, polarization converters<sup>[12–16]</sup>, modulators<sup>[17]</sup>, wave-front manipulation<sup>[18,19]</sup>, and anomalous reflection<sup>[20]</sup>. However, most reported THz metasurfaces are very limited, as their working frequency and functions are limited once they are fabricated<sup>[21]</sup>. To realize multiple functions, researchers start to design the novel metasurface structures. Gao *et al.*<sup>[22]</sup> demonstrated that an assembly of circularly polarized (CP) and linearly polarized (LP) states can be simultaneously generated by a single metasurface. Fan *et al.*<sup>[23]</sup> investigated that the cross-polarization transmission coefficient of a tri-layer chiral structure metasurface is higher than 0.9 with a fractional bandwidth of 85.7%. At the same time, multifunctional wave-front manipulation

performance is verified. Li *et al.*<sup>[24]</sup> proposed the Ge<sub>2</sub>Sb<sub>2</sub>Te<sub>5</sub> (GST)-based metasurface, which can operate as a quarter-wave plate (QWP) and a half-wave plate (HWP) in the amorphous and crystalline state for the GST, respectively. Zhang *et al.*<sup>[25]</sup> integrated graphene into a metasurface and realized a bi-functional switchable polarization converter between the QWP and HWP. Peng *et al.*<sup>[26]</sup> designed a multifunctional device with switchable absorption and polarization conversion modes by combining graphene, in which the 90% absorption is 79.5%, and the polarization conversion ratio is larger than 90%. Song *et al.*<sup>[21]</sup> presented a bifunctional design of a broadband absorber and a broadband polarization converter based on the insulator-to-metal phase transition of vanadium dioxide (VO<sub>2</sub>), in which the 90% absorption bandwidth and 90% cross-polarized reflectance are 79% and 85%, respectively. Li *et al.*<sup>[27]</sup> combined VO<sub>2</sub> and graphene to design an actively reconfigurable THz functional device with tunable absorption and electromagnetically induced transparency (EIT) window effect.

In this work, a multifunctional THz metasurface device based on VO<sub>2</sub> is proposed. When VO<sub>2</sub> is an insulator, transparency windows at 0.4465 THz and 0.639 THz are achieved due to destructive interference. When VO<sub>2</sub> is metal, the  $y$ -polarized wave can convert into the left-handed CP (LCP) wave and the right-handed CP (RCP) wave at 0.3–0.42 THz and 0.72–0.92 THz, respectively. Moreover, the effects of the incident angles and geometric parameters are also investigated. In addition, the proposed metasurface structure can be combined with Pancharatnam–Berry (P-B) phase to obtain the transmitted and reflected planar-array antenna. More interestingly, VO<sub>2</sub> in our design is a film that does not need lithography to obtain a certain pattern, which improves the convenience of fabrication and experiment. Our work provides an effective design of a multifunctional device in the THz region that has broad application in the communication system.

## 2. Design and Result

Fig. 1(a) illustrates the sketch view of our proposed THz multifunctional metasurface. As depicted in Fig. 1(b), the unit cell consists of three layers: two L-shaped metal patterns, polyimide, and VO<sub>2</sub> film. The parameters are listed in Table 1. The metal is aluminum with the conductivity of  $\sigma = 3.56 \times 10^7$  S/m in 200 nm thickness on a 50  $\mu$ m thick polyimide. The middle layer is polyimide with the permittivity of  $\epsilon = 3.5$  and the loss tangent of 0.002. For the 200 nm thick VO<sub>2</sub> film, the insulator-to-metal transition properties of VO<sub>2</sub> can be described by different values of conductivity to realize the switchability of multiple functions<sup>[21,27–32]</sup>. In our research, the conductivity of VO<sub>2</sub> is set as 200 S/m and  $2 \times 10^5$  S/m to mimic insulating state and metallic state, respectively<sup>[27,31]</sup>. In the following, we will show the

multifunctional properties of the designed metasurface based on the tunability of the VO<sub>2</sub>.

### 2.1. Dual-band EIT and linear to circular polarization converter

Figure 2(a) displays the scheme of the dual-band EIT and linear-to-circular polarization converter. Figure 2(b) shows the transmission of the proposed structure in Fig. 1 when the VO<sub>2</sub> is in the insulating state. A dual-band EIT effect is obtained in the two frequency bands: 0.35–0.5 THz and 0.6–0.85 THz, shown as a black curve in Fig. 2(b). To show the dual-band property, the spectra of the unit cell with the single small and large L shapes are represented by the dotted line and the dashed line, respectively. It is clear that the EIT effect appears both for the small L and the large L structures. The EIT peaks are located at 0.575 THz and 0.517 THz for the small and the large L structure, respectively. When we combine the two L shapes together, the dual-band EIT effect occurs. As the two excited L elements are weakly hybridized, the two EIT modes are close to their initial frequencies<sup>[33,34]</sup>.

To show the physical mechanism behind the dual-band EIT effect, the surface current distribution at the two transmission peaks  $f_1 = 0.4465$  THz and  $f_2 = 0.639$  THz is given in Fig. 2(c). It is seen that the two L shapes are excited strongly by the incident field at  $f_1$ , and an out-phase resonance appears. Therefore, the high transmission peak appears at  $f_1 = 0.4465$  THz<sup>[35]</sup>. For the EIT peak at  $f_2 = 0.639$  THz, the destructive interference between scattering electromagnetic fields of the two resonators occurs, and most energy is located at one arm of each resonator. It is worth noting that the current flows in opposite directions on the metal arms parallel to each other. Hence, the radiation loss of the metasurface is reduced significantly, and the transmission is enhanced<sup>[36]</sup>.

To further support the above assertion, the “two-particle” model is used to quantitatively describe the dual-band EIT effect. Here, two particles marked 1 and 2 represent the small and large L shape, respectively, which meet the following differential equation<sup>[37,38]</sup>:

$$x_1''(t) + \gamma_1 x_1'(t) + \omega_0^2 x_1(t) + k^2 x_2(t) = qE_0 x_2''(t) + \gamma_2 x_2'(t) + (\omega + 2\delta)^2 x_2(t) + k^2 x_1(t) = 0, \quad (1)$$

where  $x_i$ ,  $\gamma_i$  ( $i = 1$  or  $2$ ) are the amplitude and corresponding loss factor of particle 1 and particle 2,  $\delta$  and  $k$  indicate the detuning frequency and coupling strength coefficient, and  $\omega_0$  and  $q$  signify the frequency and coupling strength of the higher resonance dip with the incident wave  $E_0$ .

The simplified transmission for Eq. (1) can be obtained as

$$|T| = \frac{4\sqrt{x_{\text{eff}} + 1}}{\left(\sqrt{x_{\text{eff}} + 1} + 1\right)^2 e^{\frac{j2\pi d}{\lambda_0} \sqrt{x_{\text{eff}} + 1}} - \left(\sqrt{x_{\text{eff}} + 1} - 1\right)^2 e^{-\frac{j2\pi d}{\lambda_0} \sqrt{x_{\text{eff}} + 1}}}, \quad (2)$$

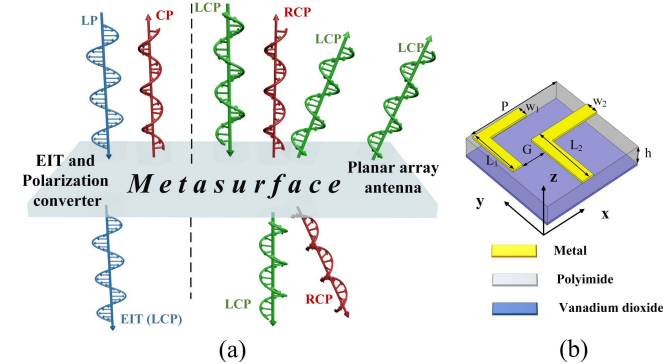
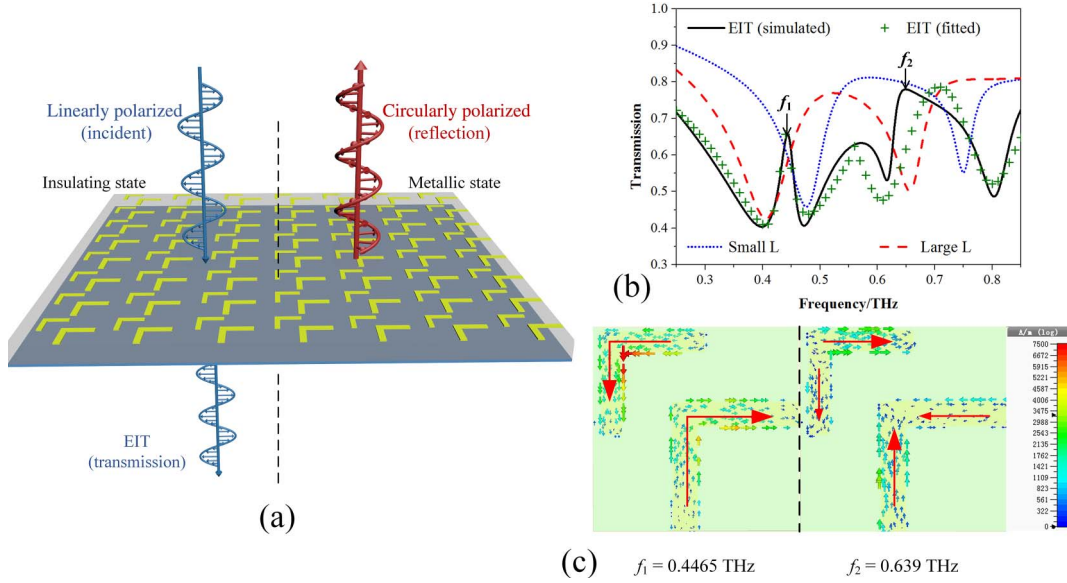


Fig. 1. (a) Sketch view and (b) unit cell of the proposed multifunctional device.

Table 1 Parameters of EIT and Polarization Converter<sup>a</sup>.

$L_1$	$L_2$	$W_1$	$W_2$	$G$
125	155	25	30	60

<sup>a</sup>Unit:  $\mu$ m.



**Fig. 2.** (a) Scheme of the dual-band EIT and linear-to-circular polarization converter. (b) Transmission curves for the metasurface with the double L (black solid), the small L (blue dotted), and the large L (red dashed) shapes when VO<sub>2</sub> is in the insulating state. The cross symbol denotes the fitted result based on the “two-particle” model. (c) The surface current distribution at the two transmission peaks.

where  $d$  is the thickness of the structure,  $\lambda_0$  is wavelength in the vacuum, and  $x_{\text{eff}}$  indicates the effective electric susceptibility of EIT effect and is expressed as

$$x_{\text{eff}} = \frac{P}{\epsilon_0 E_0} = \frac{q^2}{\epsilon_0 k^4} \frac{\omega^2 - (\omega_0 - \delta)^2 - i\gamma_2 \omega}{[\omega^2 - (\omega_0 - \delta)^2 - i\gamma_2 \omega][\omega^2 - (\omega_0 - \delta)^2 - i\gamma_1 \omega]}, \quad (3)$$

where,  $P$  is effective polarization of the metamaterial, and  $\epsilon_0$  represents permittivity in vacuum.

To verify the “two-particle” model of the dual-band EIT, two transparency windows are fitted separately and combined to form the complete curve. For the fitted analytical curve of two EIT bands, we get  $\gamma_1 = 0.1784$ ,  $\gamma_2 = 0.0141$ ,  $q = 0.6546$ ,  $k = 0.1686$ , and  $\delta = 0.9138$ . As for the second band, we set  $\gamma_1 = 0.129$ ,  $\gamma_2 = 0.166$ ,  $q = 0.55$ ,  $k = 0.36$ , and  $\delta = 0.045$ . All of the parameters above are in THz. The fitted curve (the green dots) is displayed by the cross symbols in Fig. 2(b). It is almost the same as the simulated curve, which demonstrates that the “two-particle” model can be used to explain the dual-band EIT effect.

The proposed unit cell structure behaves as a linear-to-circular polarization converter after the insulator-to-metal transition process. As demonstrated in Fig. 3(a), for the normal incident  $y$ -polarized wave, the reflective wave of the converter can be expressed as<sup>[39,40]</sup>

$$\mathbf{E}_r = E_{xr} \mathbf{e}_x + E_{yr} \mathbf{e}_y = |R_{xy}| e^{i\varphi_{xy}} E_{xi} \mathbf{e}_x + |R_{yy}| e^{i\varphi_{yy}} E_{yi} \mathbf{e}_y, \quad (4)$$

where  $R_{yy}$  and  $R_{xy}$  represent the reflection coefficient of the  $y$ - $y$  and  $x$ - $y$  polarization conversion, respectively. Correspondingly,

$\varphi_{yy}$  and  $\varphi_{xy}$  are their reflection phase. We can get the Stokes parameters as follows<sup>[25,41]</sup>:

$$\begin{aligned} I &= |R_{yy}|^2 + |R_{xy}|^2, & Q &= |R_{yy}|^2 - |R_{xy}|^2, \\ U &= 2|R_{yy}||R_{xy}|\cos\Delta\varphi, & V &= 2|R_{yy}||R_{xy}|\sin\Delta\varphi, \end{aligned}$$

where  $\Delta\varphi = \varphi_{yy} - \varphi_{xy}$ . When  $|R_{yy}| = |R_{xy}|$  and  $\Delta\varphi = 2n\pi \pm \frac{\pi}{2}$  ( $n$  is an integer) are satisfied simultaneously, the perfect linear-to-circular polarization conversion can be achieved. The normalized ellipticity is defined as  $\chi = \frac{V}{I}$  to characterize the polarization conversion performance of the designed structure, where  $\chi = +1$  and  $\chi = -1$  indicate the perfect LCP and RCP waves<sup>[42–44]</sup>.

The amplitude and phase shift of the reflection are plotted in Figs. 3(a) and 3(b). The phase difference of two components ( $R_{yy}$  and  $R_{xy}$ ) is denoted by the black solid curve in Fig. 3(b). As the shadows mark, we can see that the  $R_{yy}$  is approximately equal to  $R_{xy}$  and  $\Delta\varphi \approx \pm 90^\circ, \pm 270^\circ$  in the ranges of 0.3–0.42 THz and 0.72–0.92 THz. Based on the equation mentioned above, the normalized ellipticity is plotted in Fig. 3(c). The ellipticity is less than  $-0.88$  in the frequency range from 0.3 THz to 0.42 THz (the gray shaded region), suggesting that the LP wave is converted into an LCP wave. At the same time, the ellipticity is due to the opposite direction of the current on the two L shapes, and the electric dipole moments on both elements are canceled by each other, nearly  $+1$  in the frequency range from 0.72 THz to 0.92 THz (the yellow shaded region), meaning that the RCP wave is obtained. Therefore, the proposed structure has the dual-band linear-to-circular converter performance, with one band showing linear to LCP, and the other band showing linear

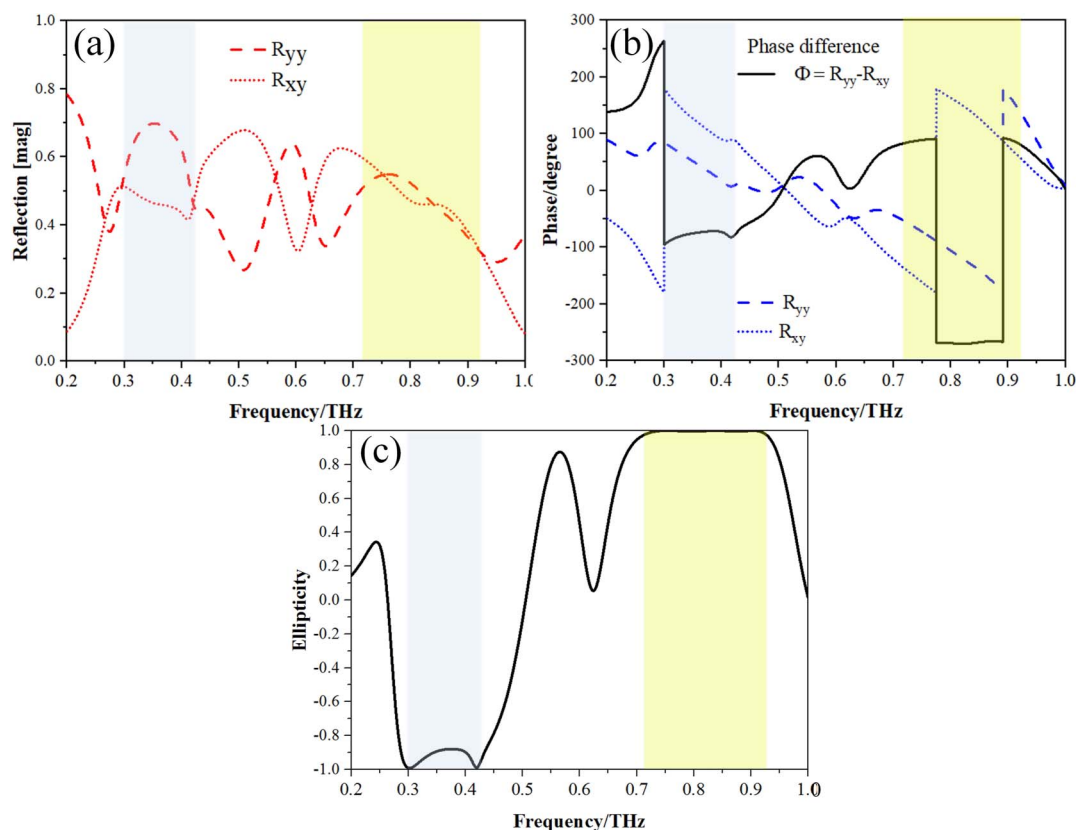


Fig. 3. (a) Reflection of  $R_{yy}$  and  $R_{xy}$ . (b) The phase and phase difference for the reflection of  $R_{yy}$  and  $R_{xy}$ . (c) The calculated ellipticity of the polarization conversion.

to RCP. The average converting efficiencies of the first and second bands are 68.7% and 94.5%, respectively.

## 2.2. Multifunctional metasurface antenna

Figure 4 shows the sketch map and basic unit cell of the multifunctional metasurface antenna with the parameters set in

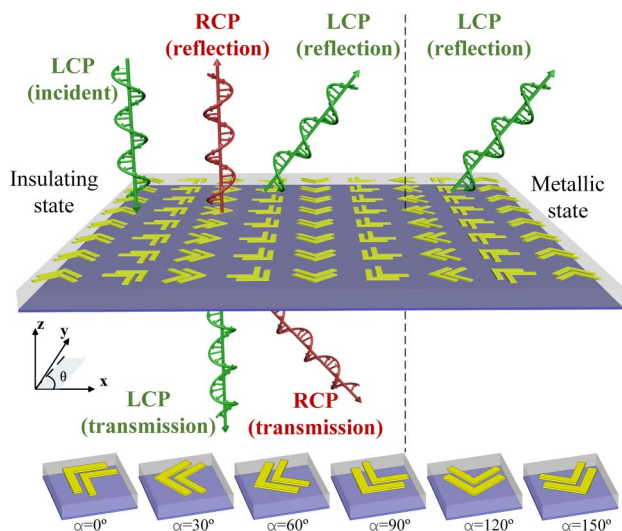


Fig. 4. Sketch map of the planar-array antenna and elements of each column.

Table 2. On the top layer, two L shapes form the unit. The bottom layer is still made of  $\text{VO}_2$ . Different from the previous design, the  $30^\circ$  rotation angle difference is given between the two adjacent unit cells. Figures 5(a) and 5(c) show the transmission and phase of the cross polarization when the  $\text{VO}_2$  is in the insulating state. In the insert, the simulated unit cells rotate counterclockwise from  $0^\circ$  to  $150^\circ$  with an interval of  $30^\circ$  and are represented by different colors from black to pink. Figures 5(b) and 5(d) show the reflection and phase of the co-polarization when the  $\text{VO}_2$  is in the metallic state. From Figs. 5(a) and 5(b), we can nearly get the same transmission and reflection of the CP wave<sup>[45,46]</sup> for the rotation unit cells with an interval of  $30^\circ$ . While in Figs. 5(c) and 5(d), the phase responds as the P-B phase<sup>[22]</sup> with phase difference of  $60^\circ$  between adjacent cells.

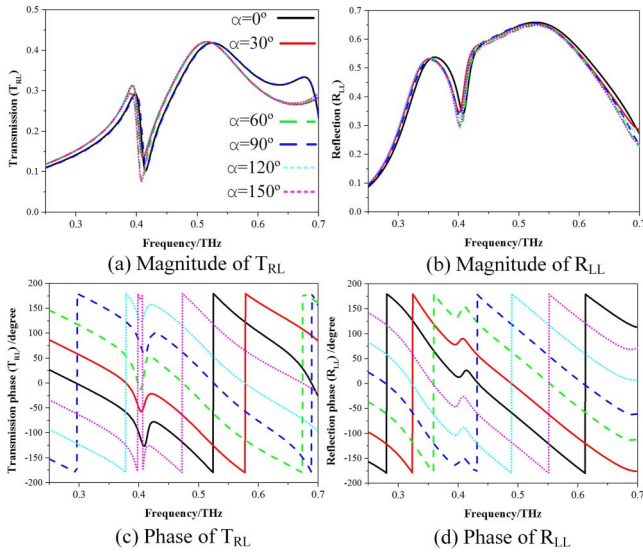
Considering the P-B phase,  $60^\circ$  phase difference for the six rotation elements could cover the  $360^\circ$  phase. The six rotation units are periodically arranged on the  $x$  axis. The abnormal reflection or transmission angles are determined by the generalized Snell's law<sup>[47–50]</sup> expressed as

Table 2 Parameters of Planar-Array Antenna<sup>a</sup>.

$L_1$	$L_2$	$W_1$	$W_2$	$G$
145	125	30	25	15

<sup>a</sup>Unit:  $\mu\text{m}$ .





**Fig. 5.** (a) Transmission and (c) phase of cross polarization for VO<sub>2</sub> in the insulating state. (b) Reflection and (d) phase of co-polarization for VO<sub>2</sub> in the metallic state.

$$\theta_{r/t} = \arcsin \frac{\lambda}{\Gamma}, \quad (5)$$

where  $\lambda$  and  $\Gamma$  are the wavelength in the free space and the total length of the structure covering the 360° phase, respectively. At a certain frequency, the abnormal angle  $\theta_r$  or  $\theta_t$  relies on  $\Gamma$ . Figure 6 shows the three- and two-dimensional radiation pattern at 0.52 THz when VO<sub>2</sub> is an insulator. We can see that the radiation energy is mainly divided into four beams under the LCP wave normal incidence. The reflection beams towards 0° and 21° are the RCP and LCP waves, respectively. The RCP

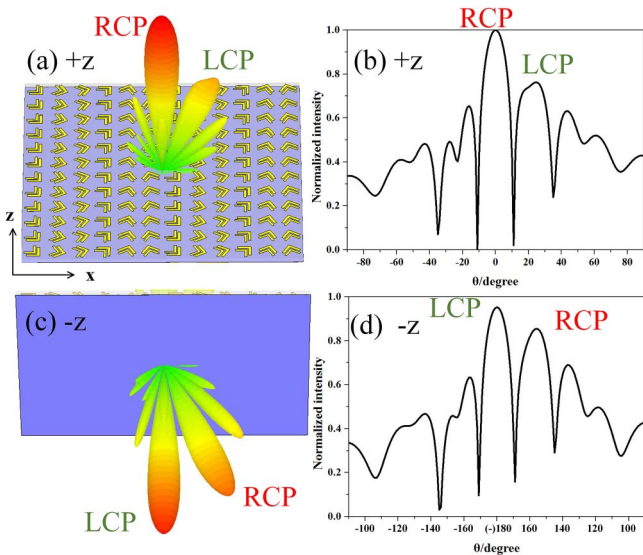


**Fig. 6.** (a) Three- and (b) two-dimensional radiation pattern of the reflected beam. (c) Three- and (d) two-dimensional radiation pattern of the transmitted beam for VO<sub>2</sub> in the insulating state.

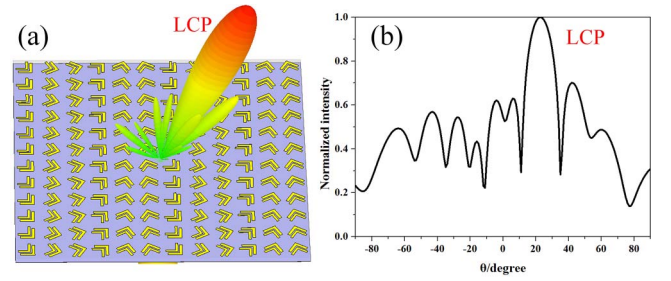


**Fig. 7.** (a) Three- and (b) two-dimensional radiation pattern of the reflected beam when VO<sub>2</sub> is in the metallic state.

wave is reflected directly, as there is no gradient phase in the cross polarization of the reflected wave. As for the LCP wave, we can calculate the abnormal angle  $\theta_r = 21.2^\circ$  based on Eq. (5), which is consistent with the simulated result. The transmission wave is also divided into the LCP wave and RCP wave with angles of 180° and 159° due to the absence of the gradient phase for the LCP wave. Therefore, when VO<sub>2</sub> is an insulator, the radiation of the LCP wave can be divided into four beams with two beams reflected and two beams transmitted<sup>[51]</sup>. These properties can be used as multifunctional antennas for CP waves.

When VO<sub>2</sub> shows a metallic state, the bottom layer acts as a metal mirror. Figures 7(a) and 7(b) demonstrate the three- and two-dimensional radiation pattern of the reflected beam at 0.52 THz. It is obvious that the co-polarized LCP wave is reflected with a 21° angle<sup>[52]</sup>, which is in agreement with the calculation result of  $\theta_r = 21.2^\circ$  based on Eq. (5). The reflected beam of the cross polarization is very weak, as the incident wave hardly undergoes polarization conversion.

### 3. Conclusion

To summarize, a multifunctional THz metasurface is presented based on the insulator-to-metal phase transition property of VO<sub>2</sub>. When VO<sub>2</sub> is an insulator, a dual-band EIT window appears at 0.4465 THz and 0.639 THz for the TE polarization. Based on the current distribution and “two-particle” model, the physical mechanism of the dual-band EIT effect has been demonstrated. When the VO<sub>2</sub> is a metal, the proposed metasurface behaves as a dual-band linear-to-circular polarization converter. The y-polarized linear wave can be effectively converted to LCP and RCP in the frequency range of 0.3–0.42 THz and 0.72–0.92 THz, respectively.

By arranging the six unit cells with the metal pattern rotating 30°, a multifunctional metasurface antenna can be obtained. When VO<sub>2</sub> is an insulator, the radiation of the LCP wave can be divided into four beams with two beams reflected and two beams transmitted. The simulation results are in agreement with the theoretical calculations. When VO<sub>2</sub> is in a metallic state, we can only get the co-polarized LCP wave reflected with a 21° angle at the same radiation frequency. Moreover, in our design, the VO<sub>2</sub> film does not need lithography to obtain certain patterns, which improves the convenience of fabrication and experiment.

Our design opens a new way for the development of multifunctional THz devices and has potential applications in the THz communication field.

## Acknowledgement

This work was supported by the National Natural Science Foundation of China (Nos. 62175016, 61875017, and 61871419), Fundamental Research Funds for the Central Universities (No. 2020RC02), Shenzhen Science and Technology Plan Basic Research Project (No. JCYJ20180305164708625), and BUPT Excellent PhD Students Foundation (No. CX2020110).

## References

1. B. Ferguson and X. Zhang, "Materials for terahertz science and technology," *Nat. Mater.* **1**, 26 (2002).
2. S. Katletz, M. Pfleger, H. Pühringer, M. Mikulics, N. Vieweg, O. Peters, B. Scherger, M. Scheller, M. Koch, and K. Wiesauer, "Polarization sensitive terahertz imaging: detection of birefringence and optical axis," *Opt. Express* **20**, 23025 (2012).
3. M. Tonouchi, "Cutting-edge terahertz technology," *Nat. Photonics* **1**, 97 (2007).
4. R. A. Shelby, D. R. Smith, and S. Schultz, "Experimental verification of a negative index of refraction," *Science* **292**, 77 (2001).
5. N. Fang, H. Lee, C. Sun, and X. Zhang, "Sub-diffraction-limited optical imaging with a silver superlens," *Science* **308**, 534 (2005).
6. C. L. Holloway, E. F. Kuester, J. A. Gordon, J. O'Hara, J. Booth, and D. R. Smith, "An overview of the theory and applications of metasurfaces: the two-dimensional equivalents of metamaterials," *IEEE Antennas Propag. Mag.* **54**, 10 (2012).
7. E. F. Kuester, M. A. Mohamed, M. Piket-May, and C. L. Holloway, "Averaged transition conditions for electromagnetic fields at a metafilm," *IEEE Trans. Antenn. Propag.* **51**, 2641 (2003).
8. Y. Fan, Y. Qian, S. Yin, D. Li, M. Jiang, X. Lin, and F. Hu, "Multi-band tunable terahertz bandpass filter based on vanadium dioxide hybrid metamaterial," *Mater. Res. Express* **6**, 055809 (2019).
9. W. Liu, Z. Dai, J. Yang, Q. Sun, C. Gong, N. Zhang, K. Ueno, and H. Misawa, "Ultrabroad and angle tunable THz filter based on multiplexed metallic bar resonators," *IEEE Photonics Technol. Lett.* **30**, 2103 (2018).
10. M. Masyukov, A. N. Grebenchukov, E. A. Litvinov, A. Baldycheva, A. V. Vozianova, and M. K. Khodzitsky, "Photo-tunable terahertz absorber based on intercalated few-layer graphene," *J. Opt.* **22**, 095105 (2020).
11. N. I. Landy, S. Sajuyigbe, J. J. Mock, D. R. Smith, and W. J. Padilla, "Perfect metamaterial absorber," *Phys. Rev. Lett.* **100**, 207402 (2008).
12. J. Hao, Y. Yuan, L. Ran, T. Jiang, J. Kong, C. Chan, and L. Zhou, "Manipulating electromagnetic wave polarizations by anisotropic metamaterials," *Phys. Rev. Lett.* **99**, 063908 (2007).
13. Y. Wei and N. Panoiu, "Polarization control using passive and active crossed graphene gratings," *Opt. Express* **26**, 1882 (2018).
14. Y. Jiang, L. Wang, J. Wang, C. N. Akwuruoha, and W. Cao, "Ultra-wideband high-efficiency reflective linear-to-circular polarization converter based on metasurface at terahertz frequencies," *Opt. Express* **25**, 27616 (2017).
15. H. Wang, Z. Zhang, K. Zhao, W. Liu, and Y. Lu, "Independent phase manipulation of co- and cross-polarizations with all-dielectric metasurface," *Chin. Opt. Lett.* **19**, 053601 (2021).
16. J. Huang, T. Fu, H. Li, Z. Shou, and X. Gao, "A reconfigurable terahertz polarization converter based on metal-graphene hybrid metasurface," *Chin. Opt. Lett.* **18**, 013102 (2020).
17. G. Zhou, P. Dai, J. Wu, B. Jin, Q. Wen, G. Zhu, Z. Shen, C. Zhang, L. Kang, W. Xu, J. Chen, and P. Wu, "Broadband and high modulation-depth THz modulator using low bias controlled VO<sub>2</sub>-integrated metasurface," *Opt. Express* **25**, 17322 (2017).
18. Z. Ma, S. M. Hanham, Y. Gong, and M. Hong, "All-dielectric reflective half-wave plate metasurface based on the anisotropic excitation of electric and magnetic dipole resonances," *Opt. Lett.* **43**, 911 (2018).
19. L. Cong, N. Xu, J. Gu, R. Singh, J. Han, and W. Zhang, "Highly flexible broadband terahertz metamaterial quarter-wave plate," *Laser Photon. Rev.* **8**, 626 (2014).
20. N. Yu, P. Genevet, M. A. Kats, F. Aieta, J.-P. Tetienne, F. Capasso, and Z. Gaburro, "Light propagation with phase discontinuities: generalized laws of reflection and refraction," *Science* **334**, 333 (2011).
21. Z. Song and J. Zhang, "Achieving broadband absorption and polarization conversion in the same frequency band," *Opt. Express* **28**, 12487 (2020).
22. Y. Gao, X. Xiong, Z. Wang, F. Chen, R. Peng, and M. Wang, "Simultaneous generation of arbitrary assembly of polarization states with geometrical-scaling-induced phase modulation," *Phys. Rev. X* **10**, 031035 (2020).
23. J. Fan and Y. Cheng, "Broadband high-efficiency cross-polarization conversion and multi-functional wavefront manipulation based on chiral structure metasurface for terahertz wave," *J. Phys. D* **53**, 025109 (2020).
24. Y. Li, J. Luo, X. Li, M. Pu, and X. Luo, "Switchable quarter-wave plate and half-wave plate based on phase-change metasurface," *IEEE Photonics J.* **12**, 4600410 (2020).
25. Z. Wei, J. Jiang, Y. Jing, L. Shuang, and L. Jiang, "Functionality-switchable terahertz polarization converter based on a graphene-integrated planar metamaterial," *OSA Continuum* **1**, 124 (2018).
26. L. Peng, X. Li, X. Gao, X. Jiang, and S. Li, "Methodology for the design of a multi-functional device with switchable absorption and polarization conversion modes by graphene and metallic metasurfaces," *Opt. Mater. Express* **9**, 687 (2019).
27. H. Li, W. Xu, Q. Cui, Y. Wang, and J. Yu, "Theoretical design of a reconfigurable broadband integrated metamaterial terahertz device," *Opt. Express* **28**, 40060 (2020).
28. Q. Wen, H. Zhang, Q. Yang, Y. Xie, K. Chen, and Y. Liu, "Terahertz metamaterials with VO<sub>2</sub> cut-wires for thermal tunability," *Appl. Phys. Lett.* **97**, 021111 (2010).
29. L. Liu, L. Kang, T. S. Mayer, and D. H. Werner, "Hybrid metamaterials for electrically triggered multifunctional control," *Nat. Commun.* **7**, 13236 (2016).
30. C. Zhang, G. Zhou, J. Wu, Y. Tang, and P. Wu, "Active control of terahertz waves using vanadium-dioxide-embedded metamaterials," *Phys. Rev. Appl.* **11**, 054016 (2019).
31. J. Zhao, J. Song, Y. Zhou, Y. Liu, and J. Zhou, "Switching between the functions of half-wave plate and quarter-wave plate simply by using a vanadium dioxide film in a terahertz metamaterial," *Chin. Phys. Lett.* **37**, 064204 (2020).
32. J. Luo, X. Shi, X. Luo, F. Hu, and G. Li, "Broadband switchable terahertz half-/quarter-wave plate based on metal-VO<sub>2</sub> metamaterials," *Opt. Express* **28**, 30861 (2020).
33. H. Zhang, Y. Cao, Y. Liu, and Y. Li, "A novel graphene metamaterial design for tunable terahertz plasmon induced transparency by two bright mode coupling," *Opt. Commun.* **391**, 9 (2017).
34. Y. Zhao, Q. Huang, H. Cai, X. Lin, H. He, H. Cheng, T. Ma, and Y. Lu, "Ultrafast control of slow light in THz electromagnetically induced transparency metasurfaces," *Chin. Opt. Lett.* **19**, 073602 (2021).
35. W. Yu, H. Meng, Z. Chen, X. Li, X. Zhang, F. Wang, Z. Wei, C. Tan, X. Huang, and S. Li, "The bright-bright and bright-dark mode coupling-based planar metamaterial for plasmonic EIT-like effect," *Opt. Commun.* **414**, 29 (2018).
36. L. Han, Q. Tan, Y. Gan, W. Zhang, and J. Xiong, "Polarization-insensitive classical electromagnetically induced transparency metamaterial with large group delay by Dirac semimetal," *Results Phys.* **19**, 103377 (2020).
37. L. Zhu, Z. Xin, L. Dong, J. Guo, J. Xun, and M. Zhong, "Polarization-independent and angle-insensitive electromagnetically induced transparent (EIT) metamaterial based on bi-air-hole dielectric resonators," *RSC Adv.* **8**, 27342 (2018).
38. F. Meng, Q. Wu, D. Erni, W. Ke, and J. Lee, "Polarization-independent metamaterial analog of electromagnetically induced transparency for a refractive-index-based sensor," *IEEE Trans. Microw. Theory Tech.* **60**, 3013 (2012).
39. A. K. Fahad, C. Ruan, and K. Chen, "Dual-wide-band dual polarization terahertz linear to circular polarization converters based on bi-layered transmissive metasurfaces," *Electronics* **8**, 869 (2019).

40. W. S. L. Lee, R. T. Ako, M. X. Low, M. Bhaskaran, S. Sriram, C. Fumeaux, and W. Withayachumnankul, "Dielectric-resonator metasurfaces for broadband terahertz quarter- and half-wave mirrors," *Opt. Express* **26**, 14392 (2018).
41. Y. Hou, C. Zhang, and C. Wang, "High-efficiency and tunable terahertz linear-to-circular polarization converters based on all-dielectric metasurfaces," *IEEE Access* **8**, 140303 (2020).
42. L. Zhu, L. Dong, J. Guo, F. Meng, X. He, C. Zha, and Q. Wu, "Polarization conversion based on Mie-type electromagnetically induced transparency (EIT) effect in all-dielectric metasurface," *Plasmonics* **13**, 1971 (2018).
43. M. Amin, O. Siddiqui, and M. Farhat, "Linear and circular dichroism in graphene-based reflectors for polarization control," *Phys. Rev. Appl.* **13**, 024046 (2020).
44. D. Yan, M. Meng, J. Li, J. Li, and X. Li, "Vanadium dioxide-assisted broadband absorption and linear-to-circular polarization conversion based on a single metasurface design for the terahertz wave," *Opt. Express* **28**, 29843 (2020).
45. J. Li and J. Yao, "Manipulation of terahertz wave using coding Pancharatnam–Berry phase metasurface," *IEEE Photonics J.* **10**, 5900512 (2018).
46. J. Li, Y. Zhang, J. Li, X. Yan, L. Liang, Z. Zhang, J. Huang, J. Li, Y. Yang, and J. Yao, "Amplitude modulation of anomalously reflected terahertz beams using all-optical active Pancharatnam–Berry coding metasurfaces," *Nanoscale* **11**, 5746 (2019).
47. Q. Zheng, Y. Li, J. Zhang, H. Ma, J. Wang, Y. Pang, Y. Han, S. Sui, Y. Shen, H. Chen, and S. Qu, "Wideband, wide-angle coding phase gradient metasurfaces based on Pancharatnam–Berry phase," *Sci. Rep.* **7**, 43543 (2017).
48. B. Xiao, F. Lan, Z. Yang, P. Mazumder, and J. Yin, "Broadband and high-efficiency circular-polarized terahertz frequency scanning metasurface," in *Photonics&Electromagnetics Research Symposium—Fall (PIERS–Fall)* (2019), p. 3229.
49. H. Zeng, F. Lan, Y. Zhang, T. Song, and Z. Yang, "Maximizing beam-scanning angle in an expected bandwidth based on terahertz metasurface with dual-mode resonance," *Appl. Phys. Express* **12**, 095501 (2019).
50. L. Wang, F. Lan, Y. Zhang, S. Liang, and P. Mazumder, "A fractional phase-coding strategy for terahertz beam patterning on digital metasurfaces," *Opt. Express* **28**, 6395 (2020).
51. S. Liu, T. Cui, L. Zhang, Q. Xu, Q. Wang, X. Wan, J. Gu, W. Tang, M. Qi, and J. Han, "Metasurfaces: convolution operations on coding metasurface to reach flexible and continuous controls of terahertz beams," *Adv. Sci.* **3**, 1600156 (2016).
52. X. Fu, F. Yang, C. Liu, X. Wu, and T. Cui, "Terahertz beam steering technologies: from phased arrays to field-programmable metasurfaces," *Adv. Opt. Mater.* **8**, 1900628 (2020).